

SQ-CBF: Signed Distance Functions for Numerically Stable Superquadric-Based Safety Filtering

Haocheng Zhao*, Lukas Brunke*, Oliver Lagerquist, Siqi Zhou, and Angela P. Schoellig

Abstract—Ensuring safe robot operation in cluttered and dynamic environments remains a fundamental challenge. While control barrier functions provide an effective framework for real-time safety filtering, their performance critically depends on the underlying geometric representation, which is often simplified, leading to either overly conservative behavior or insufficient collision coverage. Superquadrics offer an expressive way to model complex shapes using a few primitives and are increasingly used for robot safety. To integrate this representation into collision avoidance, most existing approaches directly use their implicit functions as barrier candidates. However, we identify a critical but overlooked issue in this practice: the gradients of the implicit SQ function can become severely ill-conditioned, potentially rendering the optimization infeasible and undermining reliable real-time safety filtering. To address this issue, we formulate an SQ-based safety filtering framework that uses signed distance functions as barrier candidates. Since analytical SDFs are unavailable for general SQs, we compute distances using the efficient Gilbert-Johnson-Keerthi algorithm and obtain gradients via randomized smoothing. Extensive simulation and real-world experiments demonstrate consistent collision-free manipulation in cluttered and unstructured scenes, showing robustness to challenging geometries, sensing noise, and dynamic disturbances, while improving task efficiency in teleoperation tasks. These results highlight a pathway toward safety filters that remain precise and reliable under the geometric complexity of real-world environments.

I. INTRODUCTION

A central challenge in robotics is transferring manipulators from structured laboratory settings to cluttered, dynamic real-world scenes. To operate safely alongside humans and obstacles, robots must rely on control algorithms that prevent unsafe behaviors without compromising task performance. In this context, control barrier functions (CBFs) [1] have matured into a standard tool for safety filtering [2], as they can enforce safety guarantees with low computational overhead, making them well-suited for real-time filtering in complex environments. A safety filter takes an unverified control input (e.g., from teleoperation or a motion policy) and minimizes modifications to it while ensuring safety.

*Equal contribution.

Haocheng Zhao is with the Learning Systems and Robotics Lab, Technical University of Munich, 80333 Munich, Germany. Email: haocheng.zhao@tum.de

Lukas Brunke and Angela P. Schoellig are with the Learning Systems and Robotics Lab, Technical University of Munich, 80333 Munich, Germany, also with the University of Toronto Institute for Aerospace Studies, North York, ON M3H 5T6, Canada, and also with the Vector Institute for Artificial Intelligence, Toronto, ON M5G 0C6, Canada. Emails: {lukas.brunke, angela.schoellig}@tum.de

Oliver Lagerquist is with the Learning Systems and Robotics Lab, Technical University of Munich, 80333 Munich, Germany, and also with the University of Toronto Institute for Aerospace Studies, North York, ON M3H 5T6, Canada. Email: oliver.lagerquist@mail.utoronto.ca

Siqi Zhou is with the Learning Systems and Robotics Lab, Technical University of Munich, 80333 Munich, Germany, and also with Simon Fraser University, Burnaby, BC V5A 1S6, Canada. Email: siqi@sfsu.ca

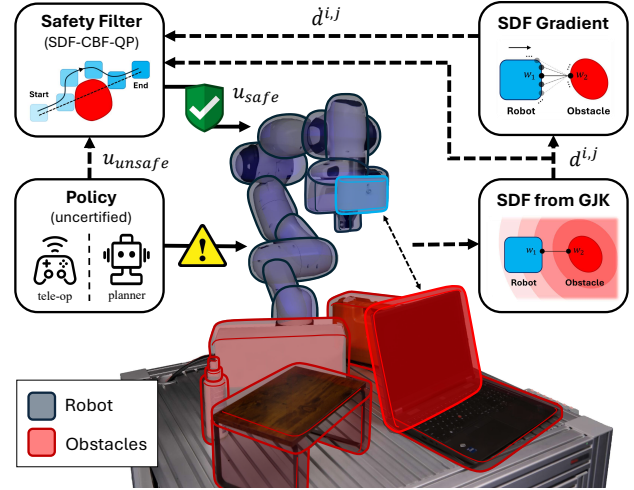


Fig. 1: Overview of the proposed SQ-CBF safety filter. The framework represents both the robot (blue) and the obstacles (red) using compact superquadrics and enforces collision avoidance through an SDF-based CBF. SDFs are computed from superquadric geometries using GJK/EPA, while well-behaved distance gradients are estimated online and incorporated into the safety filter. Given an unverified control command (e.g., from teleoperation or a planner), the safety filter modifies the command online by solving a CBF-QP, intervening only when safety is at risk. A video demonstrating the safety filter's performance can be found here: <http://tiny.cc/sq-cbf>.

However, the performance of a CBF safety filter depends heavily on how the robot and its environment are represented. Ensuring safe operation in complex environments often necessitates a trade-off between geometric fidelity and computational tractability. Simple primitives such as spheres are computationally efficient and analytically differentiable but often overly conservative, preventing the robot from reaching into tight spaces [3]. Conversely, high-fidelity representations such as Gaussian splats [4] and meshes [5] capture geometric detail but significantly increase computational burden or can yield uninformative gradients in non-convex regions, leading to oscillatory or unstable behavior.

To bridge this gap, we require a representation that is both compact and expressive. Superquadrics (SQs) [6] offer an ideal compromise, generalizing spheres, cylinders, and boxes under a unified algebraic representation while preserving differentiability. Moreover, recent advances in computer vision allow SQs to be efficiently fitted to high-dimensional sensor data [7,8]. Despite these advantages, prior works often directly use SQ's implicit function as a CBF candidate [9-11]. However, this function is not a distance metric, and its gradient norm can grow unbounded as geometries become sharp (e.g., box-like) due to the exponential terms. This leads to poor numerical conditioning of the underlying optimization [12] and can render the safety filter infeasible.

In this work, we focus on SQ-based geometric represen-

tations for CBF safety filtering in the context of collision avoidance. We adopt the signed distance function (SDF) as the CBF candidate, which maintains a gradient norm of 1 almost everywhere. Since no analytical SDF exists for generic SQs, we compute distances using the Gilbert-Johnson-Keerthi (GJK) algorithm [13] and estimate the gradients via randomized smoothing [14]. This avoids the poor conditioning of the implicit function, making safety filtering reliable. With the full pipeline illustrated in Figure 1, we summarize our contributions as follows:

- 1) We identify a long-overlooked issue in applying SQ representations to gradient-based collision avoidance: using an implicit function for collision checking is efficient but yields poorly conditioned gradients, which directly undermines the algorithm’s reliability.
- 2) To address this issue, we advocate the use of SDF as a principled alternative, and provide an efficient pipeline to compute the distance value and its gradient for SQs.
- 3) Building upon this pipeline, we propose an SQ-based CBF safety filter that uses the SDF as the CBF candidate, which translates the geometric advantages of SQs into precise and reliable collision avoidance.
- 4) We validate the proposed safety filter in teleoperation tasks through extensive simulation and real-world experiments, demonstrating its efficacy in cluttered, unstructured, and dynamic environments.

II. RELATED WORK

A. Geometric Representations for Safe Robot Control

Faithful geometric representation of the robot and environment inherently involves a trade-off between geometric fidelity and computational efficiency. A common strategy is to approximate the geometries using simple primitives such as spheres [15], capsules [3], cylinders or boxes [16], and ellipsoids [17]. Due to their limited expressiveness, such primitive-based approaches inevitably require a compromise: one must either tolerate volume over-approximation (conservative) [3], under-coverage (unsafe) [15], or require many primitives that scale poorly in optimization [4]. Conversely, high-fidelity models enable more accurate geometric reasoning and collision checking, and can be obtained from CAD meshes [5], point clouds [11,18], and volumetric maps [19]. Recently, Gaussian splatting has also emerged as an effective method for 3D reconstruction [4]. However, incorporating these representations in real-time CBF-based safety filtering often relies on additional processing (e.g., convex decomposition, translating into primitives [11], or pruning [4]) to enable efficient distance queries and well-behaved gradients.

B. Superquadrics in Robotics

In this work, we utilize SQs [6] for collision checking. Their high geometric expressiveness enables accurate representation of complex geometries with only a small number of primitives. SQs have a long history in robotics, from early use in potential-field obstacle avoidance [20] to more recent applications in drone flight [9], autonomous driving [10,21], and safe semantic manipulation [11]. Meanwhile, advances in computer vision now enable SQs to be directly recovered from point clouds [7,8] and RGB images [22], facilitating

their broader adoption in robotics. However, most prior CBF works rely on the SQ implicit function [9-11]. Although efficient to evaluate, this function is not a distance metric, and its gradient norm may become unbounded for large separations or for shape parameters approaching sharp geometries [12] (also see Figure 2). This severe numerical issue makes the implicit function unsuitable for a QP-based safety filter, as it renders the underlying optimization problem infeasible. To overcome this issue, we instead formulate the CBF using the SDF $d(\mathbf{x})$, which satisfies the eikonal equation with $\|\nabla d(\mathbf{x})\| = 1$ almost everywhere [5], yielding bounded and geometrically meaningful gradients.

C. Distance Functions and Differentiability

For simple geometries such as spheres, the SDF can be computed analytically with negligible cost, while SDF evaluation for complex geometries (e.g., superquadrics) is computationally expensive, as there are generally no closed-form solutions. Various efficient surrogates have been proposed, including local quadratic approximations [23], polynomial approximations [24], separating hyperplanes [21], and neural approximations [25]. Alternatively, for convex polyhedra, distance and penetration queries are typically computed using the GJK algorithm and the expanding polytope algorithm (EPA), respectively [13,26]. However, differentiating through GJK is challenging due to discontinuities at vertex/face transitions. While prior works approximate gradients via finite differences or conservative over-approximation [5], scaling such approaches to high-frequency control in cluttered scenes remains difficult. Our approach leverages the efficiency of GJK for distance computation but utilizes randomized smoothing [14] to extract gradients. This enables an SQ-based safety filter that is both more geometrically accurate and numerically stable.

III. PROBLEM DEFINITION

We consider the problem of ensuring real-time collision avoidance for a robot operating in a potentially changing scene, where both the robot and the obstacles are represented by geometric models for collision checking. The robot is modeled as a velocity-controlled manipulator with joint configuration $\mathbf{q} \in \mathbb{R}^n$ and kinematic model $\dot{\mathbf{q}} = \mathbf{u}$, where $\mathbf{u} \in \mathbb{R}^n$ is the joint velocity command and forward kinematics uniquely determine the poses of all attached collision geometries. Each obstacle is described by its 6D pose $\mathbf{x}_{\text{obs}} = [\mathbf{p}_{\text{obs}}^\top, \boldsymbol{\theta}_{\text{obs}}^\top]^\top \in \mathbb{R}^6$ in the world frame \mathcal{W} . These poses may change over time according to updates from perception. Let $d^{i,j}(\mathbf{q}, \mathbf{x}_{\text{obs}}^j)$ denote the signed distance between the i -th robot collision geometry and the j -th obstacle geometry, the safe set ensuring collision avoidance can be constructed as $\mathcal{S} = \{\mathbf{q} \mid d^{i,j}(\mathbf{q}, \mathbf{x}_{\text{obs}}^j) \geq 0, \forall i, j\}$.

IV. PRELIMINARIES

A. Superquadrics

Primitives such as ellipsoids, cylinders, and boxes can be generalized via SQs using only a small set of scale and shape parameters [6]. An axis-aligned SQ centered at the origin is

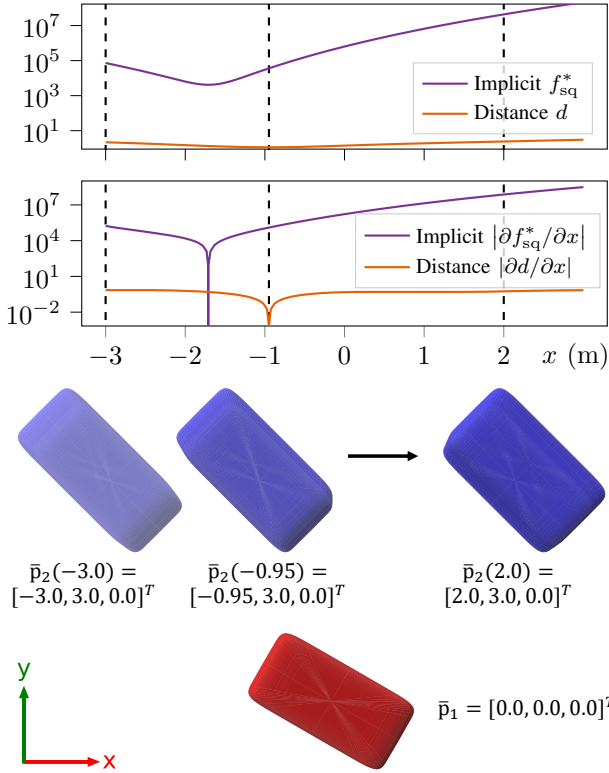


Fig. 2: Evaluating the implicit function $f_{\text{sq}}^*(x) = \min_{\mathbf{p} \in \mathbb{R}^3} f_{\text{sq}}(\mathbf{R}_z(\pi/3)^\top(\mathbf{p} - \bar{\mathbf{p}}_1), \mathbf{s}_1)$ s.t. $f_{\text{sq}}(\mathbf{R}_z(-\pi/4)^\top(\mathbf{p} - \bar{\mathbf{p}}_2(x)), \mathbf{s}_2) \leq 1$ from [17] ($\mathbf{R}_z(\varphi)$ is a rotation around the z -axis by φ) and the SDF $\bar{d}(x)$ and their gradients for two superquadrics with parameters $\mathbf{s}_1 = [0.5, 1.5, 1.0, 0.2, 0.2]^\top$ and $\mathbf{s}_2 = [1.0, 0.5, 1.0, 0.2, 0.2]^\top$ while varying their relative x position with $\bar{\mathbf{p}}_1 - \bar{\mathbf{p}}_2(x) = [0, 0, 0]^\top - [x, 3, 0]^\top$. The implicit function and its gradient are large (greater than 10^4), leading to ill-conditioned matrices in the CBF-QP. In practice, this may render the optimization infeasible or lead to oscillatory control behavior.

defined by the implicit function

$$f_{\text{sq}}(\mathbf{p}; \mathbf{s}) = \left[\left(\frac{x}{a_1} \right)^{\frac{2}{e_2}} + \left(\frac{y}{a_2} \right)^{\frac{2}{e_2}} \right]^{\frac{e_2}{e_1}} + \left(\frac{z}{a_3} \right)^{\frac{2}{e_1}} - 1, \quad (1)$$

where $\mathbf{p} = [x, y, z]^\top$ is the Cartesian coordinates and $\mathbf{s} = [a_1, a_2, a_3, e_1, e_2]^\top$ is the shape parameters. SQs are convex for $e_{1,2} \leq 2$ and become concave when $e_{1,2} > 2$. We represent the set of points on and within the SQ as the 0-superlevel set $\mathcal{S}_{\text{sq}}(\mathbf{p}; \mathbf{s}) = \{(\mathbf{p}; \mathbf{s}) : f_{\text{sq}}(\mathbf{p}; \mathbf{s}) \leq 0\}$.

As discussed in Sec. II-B, many prior works leverage SQs to enforce safety constraints as they offer an expressive representation with continuous differentiability (assuming $e_{1,2} \in (0, 2)$). However, directly using the implicit function (1) to distinguish between interior and exterior regions is undesirable in gradient-based optimization, as it leads to severe numerical instabilities: f_{sq} and its gradient may grow unboundedly. These are caused by small exponential coefficients (e_1, e_2) or when evaluating points \mathbf{p} far from the SQ's boundary $\partial\mathcal{S}_{\text{sq}}$ [12] (also see Figure 2).

B. CBF-QP Formulation

To formally guarantee safety in continuous control systems, CBFs provide a framework that ensures the system initialized within a desired set remains within the set for all future time, i.e., the set is positively forward invariant [27].

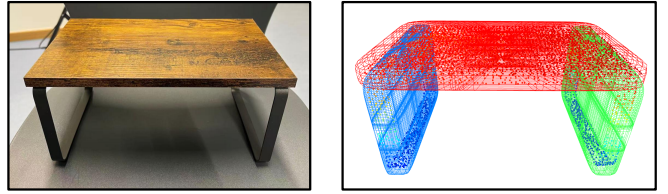


Fig. 3: Example of a real-world obstacle and its superquadric-based collision model used in our proposed safety filter framework.

Let $\mathcal{S} \subset \mathbb{R}^n$ denote a safe set defined by the 0-superlevel set of a continuously differentiable function $h : \mathbb{R}^n \rightarrow \mathbb{R}$, i.e., $\mathcal{S} = \{\mathbf{x} \in \mathbb{R}^n \mid h(\mathbf{x}) \geq 0\}$. To ensure that all trajectories starting within \mathcal{S} remain inside \mathcal{S} for all future time, the system dynamics are required to satisfy the CBF condition: $\sup_{\mathbf{u} \in \mathcal{U}} \dot{h}(\mathbf{x}, \mathbf{u}) \geq -\alpha(h(\mathbf{x}))$, where $\mathbf{u} \in \mathcal{U}$ denotes the admissible control input, $\dot{h}(\mathbf{x}, \mathbf{u})$ denotes the time derivative of $h(\mathbf{x})$, and $\alpha(\cdot)$ is an extended class- \mathcal{K} function.

In the context of safety-critical control, the safe control input can be obtained by solving a quadratic program (QP) that enforces the CBF constraint [1]:

$$\begin{aligned} \mathbf{u}^*(\mathbf{x}, \mathbf{u}_{\text{cmd}}) = \arg \min_{\mathbf{u} \in \mathcal{U}} \|\mathbf{u} - \mathbf{u}_{\text{cmd}}\|_2^2 \\ \text{s.t. } \dot{h}(\mathbf{x}, \mathbf{u}) \geq -\alpha(h(\mathbf{x})), \end{aligned} \quad (2)$$

where \mathbf{u}_{cmd} is a nominal control input. The quadratic program (2) (CBF-QP) keeps the system within the safe set \mathcal{S} while minimally altering the intended behavior.

V. METHODOLOGY

A. Robot and Environment Representation

Both the robot and the environment are represented by SQs, which provide a compact yet expressive approximation of complex scenes. The robot is modeled as a collection of SQs rigidly attached to its kinematic chain (see Table I), denoted by $\mathcal{S}_{\text{sq}}^i(\mathbf{q})$ for $i \in \mathcal{I}_{\text{sq}}^{\text{rob}} \triangleq \{1, \dots, p\}$. The i -th robot SQ is attached to link $\ell(i) \in \{1, \dots, n\}$. It is defined by a fixed local transformation relative to the link frame, parameterized by a position offset $\mathbf{p}_{\ell(i) \rightarrow i}$ and an orientation offset $\phi_{\ell(i) \rightarrow i}$. As a result, the 6D pose of each robot SQ is uniquely determined by the robot's forward kinematics. Meanwhile, obstacles in the environment are modeled as SQs with free 6D poses $\mathcal{S}_{\text{sq}}^j(\mathbf{x}_{\text{obs}}^j)$ for $j \in \mathcal{I}_{\text{sq}}^{\text{obs}} \triangleq \{1, \dots, q\}$. In practice, such obstacle SQs can be fitted based on the RGB-D point clouds from perception (see Figure 3). Note that in this work, all SQs are restricted to the convex parameter regime (i.e., $e_{1,2} \leq 2$), ensuring valid and unique signed distance and gradient computation between shapes.

B. Signed Distance Function as CBF

Consider $\mathcal{S}_{\text{sq}}^i(\mathbf{q})$ attached to the robot and $\mathcal{S}_{\text{sq}}^j(\mathbf{x}_{\text{obs}}^j)$ as a part of an obstacle, the SDF between these two convex shapes can be formulated as a constrained minimization problem over their Minkowski difference:

$$d^{i,j}(\mathbf{q}, \mathbf{x}_{\text{obs}}^j) = \begin{cases} \min_{\Delta \mathbf{p} \in \partial \mathcal{M}^{i,j}} \|\Delta \mathbf{p}\|, & \mathbf{0} \notin \mathcal{M}^{i,j}, \\ -\min_{\Delta \mathbf{p} \in \partial \mathcal{M}^{i,j}} \|\Delta \mathbf{p}\|, & \mathbf{0} \in \mathcal{M}^{i,j}, \end{cases}$$

where $\mathcal{M}^{i,j} = \{ \Delta\mathbf{p} = \mathbf{p}_1 - \mathbf{p}_2 \mid \mathbf{p}_1 \in \mathcal{S}_{\text{sq}}^i; \mathbf{p}_2 \in \mathcal{S}_{\text{sq}}^j \}$ is the Minkowski difference. Geometrically, $d^{i,j} > 0$ indicates separation between the two shapes, $d^{i,j} = 0$ corresponds to tangential contact, and $d^{i,j} < 0$ denotes interpenetration.

A CBF candidate based on $d^{i,j}$ can be formulated as

$$h_\delta^{i,j}(\mathbf{q}, \mathbf{x}_{\text{obs}}^j) = d^{i,j}(\mathbf{q}, \mathbf{x}_{\text{obs}}^j) - \epsilon_\delta,$$

where $\epsilon_\delta > 0$ denotes a prescribed safety margin. The associated CBF condition enforces a minimal safety distance by maintaining $h_\delta^{i,j} > 0$, which ensures that the two SQs remain collision-free at all times.

However, computing the signed distance between two SQs is non-trivial, as it involves solving an optimization problem over implicitly defined surfaces. For practical and efficient evaluation of the SDF, we employ the GJK algorithm and EPA [13,26], which return the minimum distance, or penetration depth, between two polytopes. We obtain a polytopic approximation for each SQ \mathcal{S}_{sq} by discretizing its surface into a dense meshgrid of points using uniform sampling [28], with n_u and n_v denoting the sampling resolutions along the longitudinal and latitudinal coordinates u and v . This enables fast, robust distance evaluation, which is subsequently integrated into the CBF constraints.

C. SDF Gradient Estimation via Randomized Smoothing

We leverage randomized smoothing to estimate the SDF gradient [14]. Consider two convex shapes \mathcal{A}_i for $i \in \{1, 2\}$ defined in their local frames \mathcal{F}_i . Let $\sigma_{\mathcal{A}}(\cdot)$ denote the support function of set \mathcal{A} and $\nabla\sigma_{\mathcal{A}}(\cdot)$ its gradient, which returns a support point on $\partial\mathcal{A}$. Let $\mathbf{x} \in \mathbb{R}^6$ parameterize the relative translation and axis-angle of frame \mathcal{F}_2 with respect to \mathcal{F}_1 , with the corresponding pose $\mathbf{T} \in SE(3)$ and its rotational component $\mathbf{R} \in SO(3)$. The optimal separation vector $\Delta\mathbf{p}^* \in \mathbb{R}^3$ expressed in \mathcal{F}_1 is defined by the stationarity condition $\mathbf{f}(\Delta\mathbf{p}^*, \mathbf{x}) = \mathbf{0}$ with

$$\mathbf{f}(\Delta\mathbf{p}^*, \mathbf{x}) = \Delta\mathbf{p}^* - \nabla\sigma_{\mathcal{A}_1}(-\Delta\mathbf{p}^*) + \mathbf{T} \nabla\sigma_{\mathcal{A}_2}(\mathbf{R}^\top \Delta\mathbf{p}^*).$$

Note that \mathbf{p}_1^* and \mathbf{p}_2^* correspond to $\Delta\mathbf{p}^*$ are the witness points on $\partial\mathcal{A}_1$ and $\partial\mathcal{A}_2$, respectively.

a) *Implicit differentiation*: By the implicit function theorem, the sensitivity of $\Delta\mathbf{p}^*$ w.r.t. \mathbf{x} is

$$\frac{\partial \Delta\mathbf{p}^*}{\partial \mathbf{x}} = -\left(\frac{\partial \mathbf{f}}{\partial \Delta\mathbf{p}^*}\right)^{-1} \frac{\partial \mathbf{f}}{\partial \mathbf{x}}.$$

The Jacobian $\partial\mathbf{f}/\partial\Delta\mathbf{p}^*$ admits the closed form:

$$\frac{\partial \mathbf{f}}{\partial \Delta\mathbf{p}^*} = \mathbf{I} + \nabla^2\sigma_{\mathcal{A}_1}(-\Delta\mathbf{p}^*) + \mathbf{R} \nabla^2\sigma_{\mathcal{A}_2}(\mathbf{R}^\top \Delta\mathbf{p}^*) \mathbf{R}^\top,$$

where $\nabla^2\sigma_{\mathcal{A}}(\cdot)$ denotes the Hessian of the support function (estimated in the following). The gradient $\partial\mathbf{f}/\partial\mathbf{x}$ is obtained by applying the chain rule, and the derivations for the gradients $\partial\mathbf{T}/\partial\mathbf{x}$ and $\partial\mathbf{R}/\partial\mathbf{x}$ can be found in [29].

b) *Smooth Hessian surrogate via local geometry*: For polyhedral or mesh-based shapes, the non-smooth support function $\sigma_{\mathcal{A}}$ always results in an ill-conditioned Hessian. To obtain a numerically stable local surrogate, we approximate $\nabla^2\sigma_{\mathcal{A}}(\mathbf{x})$ by smoothing over a finite set of neighbors [14]. Specifically, let $\mathbf{V} = [\mathbf{v}_1 \dots \mathbf{v}_{N_v}] \in \mathbb{R}^{3 \times N_v}$ collect $N_v > 1$ nearby vertex directions that encode the local surface

geometry around \mathbf{x} , and define the directional projections $\mathbf{z} = \mathbf{V}^\top \mathbf{x}$. The softmax $\mathbf{a}_\epsilon(\mathbf{z}) = \text{softmax}(\mathbf{z}/\epsilon)$ assigns smooth weights to these directions controlled by the temperature $\epsilon > 0$. Projecting the Jacobian of this softmax onto the vertex directions \mathbf{V} yields a smooth Hessian surrogate:

$$\begin{aligned} \nabla^2\sigma_{\mathcal{A}}(\mathbf{x}) &\approx \mathbf{V} \frac{\partial \mathbf{a}_\epsilon(\mathbf{z})}{\partial \mathbf{z}} \mathbf{V}^\top \\ &= \mathbf{V} \left[\frac{1}{\epsilon} (\text{diag}(\mathbf{a}_\epsilon(\mathbf{z})) - \mathbf{a}_\epsilon(\mathbf{z}) \mathbf{a}_\epsilon(\mathbf{z})^\top) \right] \mathbf{V}^\top. \end{aligned} \quad (3)$$

Intuitively, this construction replaces the non-smooth vertex-switching of the support function with a locally averaged curvature that reflects the underlying mesh geometry. To avoid the expensive outer product for large N_v , we rewrite and compute it as $\mathbf{V} \frac{\partial \mathbf{a}_\epsilon(\mathbf{z})}{\partial \mathbf{z}} \mathbf{V}^\top = \frac{1}{\epsilon} (\mathbf{V} \text{diag}(\mathbf{a}_\epsilon(\mathbf{z})) \mathbf{V}^\top - (\mathbf{V} \mathbf{a}_\epsilon(\mathbf{z})) (\mathbf{V} \mathbf{a}_\epsilon(\mathbf{z}))^\top)$.

c) *Gradient of signed distance*: The gradient of the signed distance d w.r.t. the relative pose \mathbf{x} is

$$\mathbf{J}_\mathbf{x} \triangleq \frac{\partial d}{\partial \mathbf{x}} = \text{sign}(d) \frac{\Delta\mathbf{p}^{*\top}}{\|\Delta\mathbf{p}^*\|} \frac{\partial \Delta\mathbf{p}^*}{\partial \mathbf{x}}, \quad (4)$$

where $\|\Delta\mathbf{p}^*\|$ denotes the norm of $\Delta\mathbf{p}^*$. This formulation yields an SDF gradient estimation that can be incorporated into gradient-based safety constraints.

D. Estimation of the CBF Derivative

With the randomized smoothing estimator, the CBF time derivative can be efficiently computed in closed form. The robot SQs and their motions are parameterized by \mathbf{q} and $\dot{\mathbf{q}}$, whereas each obstacle SQ $\mathcal{S}_{\text{sq}}^j$ and its motion are described by the 6D pose $\mathbf{x}_{\text{obs}}^j$ and the time derivative $\dot{\mathbf{x}}_{\text{obs}}^j$, respectively. Using the chain rule, the SDF's time derivative is

$$\dot{d}^{i,j}(\mathbf{q}, \mathbf{x}_{\text{obs}}^j) = \mathbf{J}_{\mathbf{x}^i}^{i,j} \dot{\mathbf{x}}_{\text{rob}}^i(\mathbf{q}) + \mathbf{J}_{\mathbf{x}^j}^{i,j} \dot{\mathbf{x}}_{\text{obs}}^j,$$

where $\mathbf{J}_{\mathbf{x}^i}^{i,j} = \frac{\partial d^{i,j}}{\partial \mathbf{x}_{\text{rob}}^i}$ and $\mathbf{J}_{\mathbf{x}^j}^{i,j} = \frac{\partial d^{i,j}}{\partial \mathbf{x}_{\text{obs}}^j}$ capture the sensitivity of the signed distance to state changes and can be efficiently estimated with (4). While the obstacle state $\mathbf{x}_{\text{obs}}^j$ and its time derivative $\dot{\mathbf{x}}_{\text{obs}}^j$ can be directly obtained from the perception pipeline, the state rates of robot SQ $\dot{\mathbf{x}}_{\text{rob}}^i$ must be obtained from the robot's joint velocities $\dot{\mathbf{q}}$.

Specifically, for the i -th SQ attached to link $\ell(i)$, we map the joint velocities to the SQ's analytical state derivative using a two-stage kinematic transformation. First, we map the joint velocities to the spatial twist:

$$\begin{bmatrix} \mathbf{v}_{\ell(i)} \\ \boldsymbol{\omega}_{\ell(i)} \end{bmatrix} = \mathbf{J}_{\ell(i)}(\mathbf{q}) \dot{\mathbf{q}} = \begin{bmatrix} \mathbf{J}_{\ell(i)}^v(\mathbf{q}) \\ \mathbf{J}_{\ell(i)}^\omega(\mathbf{q}) \end{bmatrix} \dot{\mathbf{q}},$$

where $\mathbf{J}_{\ell(i)}(\mathbf{q})$ denotes the geometric Jacobian up to link $\ell(i)$ [30]. Second, we transform the resulting twist into the analytical state derivative of the attached SQ:

$$\dot{\mathbf{x}}_{\text{rob}}^i = \mathbf{X}_{\ell(i) \rightarrow i} \begin{bmatrix} \mathbf{v}_{\ell(i)} \\ \boldsymbol{\omega}_{\ell(i)} \end{bmatrix} = \begin{bmatrix} \mathbf{I}_3 & -[\mathbf{p}_{\ell(i) \rightarrow i}] \times \\ \mathbf{0}_3 & \mathbf{J}_l^{-1}(\boldsymbol{\phi}_{\ell(i) \rightarrow i}) \end{bmatrix} \begin{bmatrix} \mathbf{v}_{\ell(i)} \\ \boldsymbol{\omega}_{\ell(i)} \end{bmatrix},$$

where $[\cdot] \times$ is the skew-symmetric operator, $\mathbf{X}_{\ell(i) \rightarrow i}$ represents the local transformation from link frame to SQ frame, and $\mathbf{J}_l(\cdot)$ is the left Jacobian of $SO(3)$ [29].

By choosing $u = \dot{q}$, the SDF-CBF condition can be compactly written as

$$\mathbf{J}_{\delta|i}^{i,j} \mathbf{u} + \dot{d}_{\text{obs}}^{i,j} \geq -\alpha_\delta(h_\delta^{i,j}),$$

where $\mathbf{J}_{\delta|i}^{i,j} = \mathbf{J}_{\mathbf{x}^i}^{i,j} \mathbf{X}_{\ell(i) \rightarrow i} \mathbf{J}_{\ell(i)}$, $\dot{d}_{\text{obs}}^{i,j} = \mathbf{J}_{\mathbf{x}^j}^{i,j} \dot{\mathbf{x}}_{\text{obs}}^j$, and α_δ is a class- \mathcal{K} function. We evaluate the derivative estimation in detail in Sec. VI-C.

E. Safety Filter Formulation

To improve task-space command tracking [15], we augment the CBF-QP objective (2) with a task-consistency term that penalizes deviations in both joint space and task space:

$$\|\mathbf{u} - \mathbf{u}_{\text{cmd}}\|_2^2 + \|\mathbf{J}(\mathbf{q})(\mathbf{u} - \mathbf{u}_{\text{cmd}})\|_2^2.$$

This formulation effectively regularizes the control input in the task space, promoting adherence to the commanded task-space motion while allowing flexibility in the joint space.

In the context of manipulation, we observed that the safety filter may occasionally drive the robot toward kinematic singularities due to null-space motions. To mitigate this issue, we could additionally incorporate a manipulability-based CBF for singularity avoidance in the related tasks. The manipulability index

$$\mu(\mathbf{q}) = \sqrt{\det(\mathbf{J}(\mathbf{q}) \mathbf{J}^\top(\mathbf{q}))}$$

provides a measure of local kinematic dexterity. Larger values indicate higher manipulability, and $\mu(\mathbf{q}) = 0$ corresponds to a kinematic singularity [31]. Based on $\mu(\mathbf{q})$, a CBF for singularity avoidance can be constructed as

$$h_\mu(\mathbf{q}) = \mu(\mathbf{q}) - \epsilon_\mu,$$

where $\epsilon_\mu > 0$ is a user-defined threshold. Enforcing the condition $h_\mu(\mathbf{q}) \geq 0$ ensures that the robot remains sufficiently far from kinematic singularities during execution. The manipulability index is smooth for $\mu(\mathbf{q}) > 0$, and its time derivative can be written as $\dot{\mu} = \mathbf{J}_\mu(\mathbf{q}) \dot{\mathbf{q}}$, where $\mathbf{J}_\mu(\mathbf{q})$ denotes the manipulability Jacobian [32].

With all the definitions above, collision avoidance and singularity avoidance are jointly enforced by solving a single quadratic program at each control cycle:

$$\begin{aligned} \mathbf{u}^* = \arg \min_{\mathbf{u} \in \mathcal{U}} & \|\mathbf{J}(\mathbf{q})(\mathbf{u} - \mathbf{u}_{\text{cmd}})\|_2^2 + \|\mathbf{u} - \mathbf{u}_{\text{cmd}}\|_2^2 \quad (5) \\ \text{s.t. } & \mathbf{J}_{\delta|i}^{i,j} \mathbf{u} + \dot{d}_{\text{obs}}^{i,j} \geq -\alpha_\delta(h_\delta^{i,j}), \quad \forall (i, j) \in \mathcal{P}_{\text{env}}, \\ & (\mathbf{J}_{\delta|i}^{i,j} + \mathbf{J}_{\delta|j}^{i,j}) \mathbf{u} \geq -\alpha_\delta(h_\delta^{i,j}), \quad \forall (i, j) \in \mathcal{P}_{\text{self}}, \\ & \mathbf{J}_\mu \mathbf{u} \geq -\alpha_\mu(h_\mu), \end{aligned}$$

where we have dropped function arguments for brevity, $\mathcal{P}_{\text{env}} = \mathcal{I}_{\text{sq}}^{\text{rob}} \times \mathcal{I}_{\text{sq}}^{\text{obs}}$, and $\mathcal{P}_{\text{self}} \subset \mathcal{I}_{\text{sq}}^{\text{rob}} \times \mathcal{I}_{\text{sq}}^{\text{rob}}$ is the set of robot SQ pairs considered for self-collision avoidance. The resulting optimization problem can be solved efficiently online using standard QP solvers, allowing the proposed safety filter to operate in real time even in cluttered environments with many collision geometries.

VI. EXPERIMENTS

In this section, we present the experimental evaluation of the proposed safety filter. We begin by addressing two key questions: (i) how expressive and compact the proposed superquadric collision model is compared to existing representations, and (ii) whether accurate SDF gradients can be obtained online for reliable safety filtering. We then present simulation and real-world results demonstrating the safety filter's behavior in tabletop manipulation scenarios.

A. Implementation Details

We compute the pairwise distances via the GJK/EPA algorithm integrated in the Coal library [33]. Each SQ's surface is uniformly sampled with $n_u = n_v = 200$ to obtain a dense mesh representation. We construct a k -d tree to accelerate nearest-vertex queries during witness-point extraction, significantly reducing the query time per SDF evaluation. For gradient estimation, a local neighborhood of vertices of depth 8 around the witness point is considered [14].

All simulation and real-world experiments are conducted on a workstation equipped with an Intel Core Ultra 9 285K CPU. We select $\epsilon = 10^{-8}$ unless stated otherwise. For the SDF-CBF, we choose $\alpha_\delta(\rho) = 1.5\rho$ and set the safety margin $\epsilon_\delta = 0.01$. We select $\alpha_\mu(\rho) = 0.1\rho$ and threshold $\epsilon_\mu = 0.02$ for the manipulability-CBF. In the real-world experiments, we additionally penalize input discontinuity using $w\|\mathbf{u}_k - \mathbf{u}_{k-1}\|_2^2$ with $w = 0.1$. We solve the complete CBF-QP (5) at a control frequency of 100 Hz.

B. Collision Model Representation

We compare the proposed SQ-based representation with: (i) sphere-based models [15] and (ii) cylinder-box decompositions [16]. We also include the official FR3 collision model [34] for reference. The comparison considers: (i) number of primitives, (ii) coverage and over-approximation, and (iii) smoothness and convexity. The first two assess geometric compactness and fidelity, while the latter ensure reliable gradient evaluation in CBF-based filtering.

We denote the true robot geometry by $\mathcal{R} \subset \mathbb{R}^3$ and the fitted collision model by $\mathcal{C} \subset \mathbb{R}^3$. The coverage and over-approximation ratios are computed using a voxel discretization. Let $\Omega \subset \mathbb{R}^3$ be a region that contains $\mathcal{R} \cup \mathcal{C}$. A uniform discretization of Ω with resolution $\Delta = 0.005$ m yields the voxel set Ω_Δ . Then the voxelized robot and collision model geometries are $\mathcal{V}_\mathcal{R} = \{v_i \in \Omega_\Delta \mid v_i \cap \mathcal{R} \neq \emptyset\}$ and $\mathcal{V}_\mathcal{C} = \{v_i \in \Omega_\Delta \mid v_i \cap \mathcal{C} \neq \emptyset\}$, respectively. The coverage and over-approximation ratios are defined as

$$\text{Coverage} = \frac{|\mathcal{V}_\mathcal{R} \cap \mathcal{V}_\mathcal{C}|}{|\mathcal{V}_\mathcal{R}|}, \quad \text{OverApprox} = \frac{|\mathcal{V}_\mathcal{C} \setminus \mathcal{V}_\mathcal{R}|}{|\mathcal{V}_\mathcal{R}|}.$$

The comparison of collision models is summarized in Table I. The sphere-based model is least conservative but provides less than 60% coverage, as spheres poorly capture thin structures and sharp features, leading to missed collisions (see Sec. VI-D). The cylinder-box decomposition achieves near-complete coverage but incurs almost 50% over-approximation and requires additional smoothing for gradient-based optimization [16]. In contrast, the proposed SQ-based model balances coverage and conservativeness: it

TABLE I: Comparison of geometric collision models. Bold entries are from our proposed method, while red entries highlight notable limitations.

Representation	Sphere [15]	Cylinder & Box [16]	Superquadric (ours)	FR3 Collision Mesh [34]
Illustration				
Geometry Count	21 Spheres	11 Cylinders + 4 Boxes	15 Superquadrics	9 Tri. Meshes + 8 Boxes
Coverage (\uparrow)	59.08%	99.00%	97.14%	97.28%
OverApprox. (\downarrow)	2.57%	45.23%	28.69%	1.92%
Smoothness	smooth	not smooth	smooth[†]	not smooth
Convexity	convex	convex	convex[‡]	non-convex

[†] A superquadric is smooth when the shape exponent satisfies $0 < e_{1,2} < 2$.

[‡] A superquadric is convex when the shape exponent satisfies $e_{1,2} \leq 2$.

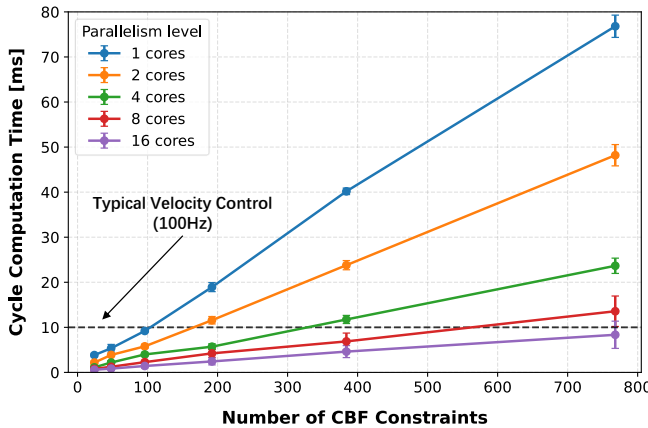


Fig. 4: Mean cycle time (error bars represent three standard deviations) of the proposed SDF and gradient evaluation pipeline as a function of the number of CBF constraints under different CPU parallelization levels. Multi-core execution significantly improves scalability, enabling real-time (100 Hz) velocity control with hundreds of collision constraints.

achieves coverage comparable to the official FR3 collision model, reduces over-approximation relative to the cylinder-box approach, and uses fewer geometries. Moreover, SQs are smooth and convex by construction (for $e_{1,2} \in (0, 2)$), ensuring differentiable SDFs and making the representation well-suited for the proposed CBF-QP safety filter.

C. SDF Gradient Estimation

a) *Computational Efficiency*: Figure 4 shows the mean cycle time with three standard deviations versus the number of CBF constraints under different CPU parallelization levels. On a single CPU core, the cycle time grows approximately linearly with the number of CBF constraints. Beyond 96 constraints, the cycle time exceeds the 10 ms budget required for 100 Hz control. Since our approach is amenable to multi-core parallelization, we can significantly reduce the computation time. With four parallel processes, we sustain more than 300 collision pairs within the 10 ms budget, while 16 cores scale this further to around 800 pairs, highlighting the strong parallel scalability of the proposed approach.

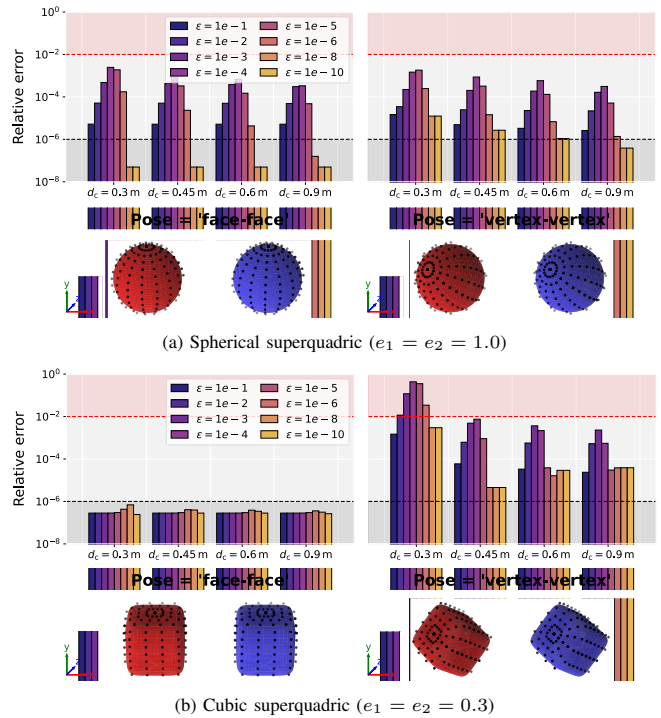


Fig. 5: Accuracy of the gradient estimation for different centroid distances d_c and temperature values ε . The relative error (logarithmic scale) of the estimated gradient (x -component) is evaluated against ground-truth gradients for two representative SQ pairs: (a) sphere-sphere and (b) cube-cube. Results are reported for different relative orientations (face-face and vertex-vertex). The accuracy is sensitive to temperature ε in all cases except face-face cubes. This highlights the importance of selecting an appropriate temperature ε to achieve sufficiently accurate gradient estimates.

b) *Gradient Estimation Accuracy*: In Figure 5, we assess how the temperature ε , shape parameters $e_{1,2}$, centroid distance d_c , and relative pose affect the accuracy of the SDF gradient estimation. The metric is chosen as the relative error between the estimated gradient and the ground truth value. The ground truth SDFs are computed by solving a constrained optimization with IPOPT (tolerance 10^{-8}), and the corresponding gradients via central differences (step 10^{-6}). Only the x -component is reported, as it captures the trends across all dimensions. We compare sphere-sphere

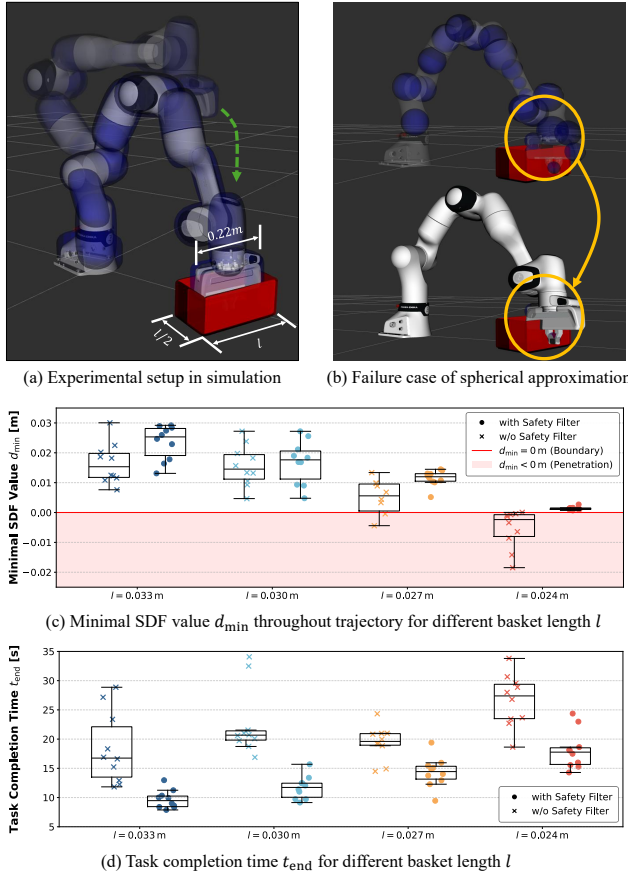


Fig. 6: Simulation experiment of a teleoperated insertion task under progressively tighter geometric constraints. We compare executions with and without safety filtering and using different collision models. The results show that the proposed superquadric-based safety filter consistently prevents collisions and improves task efficiency by 39% on average. In contrast, the coarse spherical model from [15] may be insufficient to guarantee safety.

($e_{1,2} = 1.0$) and cube–cube ($e_{1,2} = 0.3$) pairs in face–face and vertex–vertex configurations (see Figure 5) with $a_{1,2,3} = 0.1$. We established an acceptable threshold of 1% (red dashed line), while errors below 10^{-6} are treated as numerical noise due to the differentiation step size.

Figure 5a shows that, for spherical SQs, the relative pose has little influence on gradient estimation error, as expected from rotational symmetry. The observed fluctuations are caused by the inhomogeneous vertex distribution in different orientations. In contrast, the error is clearly sensitive to the temperature parameter ε , with both very small and very large values yielding lower errors, and best results for $\varepsilon \in \{10^{-8}, 10^{-10}\}$. For rounded cubes (Figure 5b), the behavior differs between configurations: the face-face case is largely insensitive to centroid distance and temperature, whereas the vertex–vertex case is strongly affected by both. In particular, at the smallest centroid distance $d_c = 0.3$, the error exceeds the acceptable 1% threshold for several temperature values. Based on this study, we adopt $\varepsilon \leq 10^{-8}$, which consistently yields acceptable accuracy across shapes, distances, and orientations.

D. Simulation Experiments

We evaluate the proposed safety filter in simulation to assess its safety and efficiency in challenging environments,

particularly when the robot must move in close proximity to obstacles and overly conservative behaviors may degrade task performance. As shown in Figure 6a, the robot performs a teleoperated insertion into a basket-like container with side lengths l and $l/2$. Decreasing l reduces clearance and increases task difficulty. In the most challenging configuration ($l = 0.24$ m), the end-effector has only 0.005 m one-sided clearance. To maintain feasibility in these highly constrained settings, the safety margin is reduced to $\epsilon_\delta = 0.005$ and 0.0025 for the second-to-last and last configuration, respectively. Safety is quantified by the minimum signed distance d_{\min} along each trial ($d_{\min} < 0$ indicates penetration), and efficiency by the task completion time t_{end} . Each configuration was evaluated through a comparative user study comprising ten teleoperated trials, both with and without the safety filter. We used fixed random seeds to generate identical obstacle positions across pairs of trials, ensuring a fair comparison.

Figure 6b shows a representative failure case of safety filtering when using a spherical approximation, where collisions occur due to insufficient geometric fidelity (e.g., approximation used in [15]). In contrast, Figure 6c shows that the proposed SQ-based safety filter maintains strictly positive SDF values across all tested configurations, while executions without the safety filter frequently result in penetration in highly constrained settings. Importantly, safety does not come at the expense of efficiency. As shown in Figure 6d, our proposed safety filter reduces task completion time by 39% on average across all difficulty levels. This improvement arises because users no longer need to repeatedly pause and adjust the end-effector to avoid contact with the basket walls. Instead, collision avoidance is handled online by the safety filter, enabling smoother and more direct task execution.

E. Real-World Experiments

To validate the proposed safety filter in real-world settings, we design three representative manipulation tasks covering different sources of geometric complexity:

- **OBJECT HANDOVER IN TIGHT SPACES:** three wooden beams restrict the workspace while the robot receives and hands over a tennis ball, evaluating whole-body collision avoidance across all robot links.
- **OBJECT TRANSPORTATION IN UNSTRUCTURED SCENES:** the robot grasps a spray bottle and transports it through a narrow passage formed by unstructured obstacles, assessing collision avoidance for both the end-effector and the grasped object.
- **MANIPULATION WITH DYNAMIC OBSTACLES:** The robot moves a chess piece and presses the timer button, while avoiding a stick swung by a human nearby, validating reactive avoidance in dynamic scenes.

We deploy our proposed safety filter in a closed loop with a Franka Emika FR3 robotic manipulator to prevent potentially unsafe commands issued by a non-expert teleoperator. Low-level robot control is handled using the CRISP framework [35], which provides joint-state feedback and translates certified joint-velocity commands into motor torques. We use a wrist-mounted Femto Bolt RGB-D camera to capture scene-level point clouds of static objects. We further



Fig. 7: Real-world teleoperated manipulation experiments demonstrating the efficacy of our proposed safety filter on three representative tasks. Across all tasks, the safety filter consistently enables collision-free execution with minimal intervention, despite tight geometric constraints, unstructured and cluttered obstacles, and dynamic disturbances. A video demonstrating the safety filter’s performance can be found here: <http://tiny.cc/sq-cbf>.

process this into an object-level point cloud [36]. To align these segmented observations with their corresponding object models, the trimmed iterative closest point algorithm [37] is employed to register the partial point clouds to known complete object point clouds. For dynamic scenarios, obstacle poses are obtained via motion capture, and an extended Kalman filter is used to estimate their velocity states for reactive collision avoidance.

Representative trials from each task are depicted in Figure 7 and can be found in this video <http://tiny.cc/sq-cbf>. The safety filter enables collision-free execution across all tasks despite tight geometric constraints, unstructured and cluttered obstacles, dynamic disturbances, and sensing noise in real-world perception. During handover and narrow-passage tasks, the safety filter effectively regulates whole-body motion to avoid contact with surrounding obstacles, while in the dynamic task, the filter reacts online to human-induced motion. In all three experiments, collision avoidance is achieved with a 100% success rate across trials with only minimal modification to teleoperation commands, demonstrating the robustness and practical applicability of the proposed approach in real-world settings.

VII. CONCLUSION

In this work, we presented a geometry-aware safety filter that combines expressive SQ-based collision models with an SDF-based formulation. By resolving the numerical issues inherent to implicit superquadric functions, the proposed approach bridges the gap between high-fidelity geometric modeling and reliable, real-time gradient-based safety filtering. Extensive simulations and real-world experiments demonstrate that the proposed safety filter consistently achieves collision-free execution under challenging geometric conditions, sensing noise, and dynamic disturbances, while also improving task efficiency in teleoperated manipulation by reducing unnecessary corrective motions.

REFERENCES

- [1] A. D. Ames *et al.*, “Control barrier functions: Theory and applications,” in *Proc. of the Euro. Ctrl. Conf. (ECC)*, 2019, pp. 3420–3431.
- [2] L. Brunke *et al.*, “Safe learning in robotics: From learning-based control to safe reinforcement learning,” *Annual Review of Control, Robotics, and Autonomous Systems*, vol. 5, pp. 411–444, 2022.
- [3] S. Zimmermann *et al.*, “Differentiable collision avoidance using collision primitives,” in *Proc. of the Inter. Conf. on Intel. Rob. and Sys. (IROS)*, 2022, pp. 8086–8093.
- [4] T. Chen *et al.*, “A control barrier function for safe navigation with online gaussian splatting maps,” in *Proc. of the Inter. Conf. on Robot. and Auto. (ICRA)*, 2025, pp. 11758–11765.
- [5] A. Singletary *et al.*, “Safety-critical manipulation for collision-free food preparation,” *IEEE Robot. and Auto. Lett.*, vol. 7, no. 4, pp. 10954–10961, 2022.
- [6] Barr, “Superquadrics and angle-preserving transformations,” *IEEE Computer Graphics and Applications*, vol. 1, no. 1, pp. 11–23, 1981.
- [7] W. Liu *et al.*, “Robust and accurate superquadric recovery: a probabilistic approach,” in *Proc. of the Conf. on Comp. Vis. and Patt. Recog. (CVPR)*, 2022, pp. 2666–2675.
- [8] E. Fedele *et al.*, “SuperDec: 3D Scene Decomposition with Superquadric Primitives,” in *Proc. of the Inter. Conf. on Comp. Vision (ICCV)*, 2025.
- [9] B. Xu and K. Sreenath, “Safe teleoperation of dynamic uavs through control barrier functions,” in *Proc. of the Inter. Conf. on Robot. and Auto. (ICRA)*, 2018, pp. 7848–7855.
- [10] W. Xiao *et al.*, “Barriernet: Differentiable control barrier functions for learning of safe robot control,” *IEEE Trans. on Robotics*, vol. 39, no. 3, pp. 2289–2307, 2023.
- [11] L. Brunke *et al.*, “Semantically safe robot manipulation: From semantic scene understanding to motion safeguards,” *IEEE Robot. and Auto. Lett.*, vol. 10, no. 5, pp. 4810–4817, 2025.
- [12] N. Vaskevicius and A. Birk, “Revisiting superquadric fitting: A numerically stable formulation,” *IEEE Trans. on Patt. Analysis and Machine Intel.*, vol. 41, no. 1, pp. 220–233, 2019.
- [13] E. Gilbert, D. Johnson, and S. Keerthi, “A fast procedure for computing the distance between complex objects in three-dimensional space,” *IEEE Robot. and Auto. Lett.*, vol. 4, no. 2, pp. 193–203, 1988.
- [14] L. Montaut *et al.*, “Differentiable collision detection: a randomized smoothing approach,” in *Proc. of the Inter. Conf. on Robot. and Auto. (ICRA)*, 2023, pp. 3240–3246.
- [15] D. Morton and M. Pavone, “Safe, task-consistent manipulation with operational space control barrier functions,” in *Proc. of the Inter. Conf. on Intel. Rob. and Sys. (IROS)*, 2025, pp. 187–194.
- [16] V. M. Gonçalves, A. Tzes, F. Khorrami, and P. Fraisse, “Smooth distances for second-order kinematic robot control,” *IEEE Trans. on Robotics*, vol. 40, pp. 2950–2966, 2024.
- [17] B. Dai *et al.*, “Safe navigation and obstacle avoidance using differentiable optimization based control barrier functions,” *IEEE Robot. and Auto. Lett.*, vol. 8, no. 9, pp. 5376–5383, 2023.
- [18] M. De Sa *et al.*, “Point cloud-based control barrier function regression for safe and efficient vision-based control,” in *Proc. of the Inter. Conf. on Robot. and Auto. (ICRA)*, 2024, pp. 366–372.
- [19] S. Zhou, S. Papatheodorou, S. Leutenegger, and A. P. Schoellig, “Control-barrier-aided teleoperation with visual-inertial slam for safe may navigation in complex environments,” in *Proc. of the Inter. Conf. on Robot. and Auto. (ICRA)*, 2024, pp. 17836–17842.
- [20] O. Khatib, “Real-time obstacle avoidance for manipulators and mobile robots,” in *Proc. of the Inter. Conf. on Robot. and Auto. (ICRA)*, vol. 2, 1985, pp. 500–505.
- [21] Z. Wu and L. Liu, “Collision-free control barrier functions for general ellipsoids via separating hyperplane,” in *Proc. of the Inter. Conf. on Intel. Rob. and Sys. (IROS)*, 2025, pp. 19637–19644.
- [22] Z. Gao *et al.*, “Self-supervised learning of hybrid part-aware 3d representations of 2d gaussians and superquadrics,” in *Proc. of the Inter. Conf. on Comp. Vision (ICCV)*, October 2025, pp. 9649–9659.
- [23] X. Ding *et al.*, “Online control barrier function construction for safety-critical motion control of manipulators,” *IEEE Trans. on Systems, Man, and Cyber.*, vol. 54, no. 8, pp. 4761–4771, 2024.
- [24] Y. Li *et al.*, “Representing robot geometry as distance fields: Applications to whole-body manipulation,” in *Proc. of the Inter. Conf. on Robot. and Auto. (ICRA)*, 2024, pp. 15351–15357.
- [25] M. Harms *et al.*, “Neural control barrier functions for safe navigation,” in *Proc. of the Inter. Conf. on Intel. Rob. and Sys. (IROS)*, 2024, pp. 10415–10422.
- [26] G. van den Bergen, *Collision Detection in Interactive 3D Environments*. Morgan Kaufmann, 2004.

- [27] A. D. Ames, J. W. Grizzle, and P. Tabuada, “Control barrier function based quadratic programs with application to adaptive cruise control,” in *Proc. of the Conf. on Dec. and Ctrl. (CDC)*, 2014, pp. 6271–6278.
- [28] M. Pilu and R. Fisher, “Equal-distance sampling of superellipse models,” 08 1995.
- [29] J. Solà, J. Deray, and D. Atchuthan. (2018) A micro lie theory for state estimation in robotics.
- [30] K. M. Lynch and F. C. Park, *Velocity Kinematics and Statics*. Cambridge University Press, 2017, p. 146–186.
- [31] T. Yoshikawa, “Manipulability of robotic mechanisms,” *The Inter. Journal of Robotics Research*, vol. 4, no. 2, pp. 3–9, 1985.
- [32] V. Kurtz, P. Wensing, and H. Lin, “Control barrier functions for singularity avoidance in passivity-based manipulator control,” in *Proc. of the Conf. on Dec. and Ctrl. (CDC)*, 2021, pp. 6125–6130.
- [33] J. Pan *et al.*, “Coal: an extension of the flexible collision library,” <https://github.com/coal-library/coal>, 2015–2024.
- [34] Franka Emika GmbH, “FR3: Robot description and collision models,” https://github.com/frankarobotics/franka_description, 2024.
- [35] D. San José Pro *et al.*, “CRISP - compliant ROS2 controllers for learning-based manipulation policies and teleoperation,” 2025.
- [36] B. Bogenberger *et al.*, “Where did I leave my glasses? Open-vocabulary semantic exploration in real-world semi-static environments,” *IEEE Robot. and Auto. Lett.*, pp. 1–8, 2026.
- [37] D. Chetverikov, D. Svirko, D. Stepanov, and P. Krsek, “The trimmed iterative closest point algorithm,” in *Proc. of the Inter. Conf. on Patt. Recog.*, vol. 3, 2002, pp. 545–548 vol.3.